GPPS | JOURNAL

JOURNAL OF THE GLOBAL POWER AND PROPULSION SOCIETY
journal.gpps.global

Dynamic flow distortions in a highly bent engine intake: A comparative analysis of compressor influence on flow distortion characteristic

Original article

Article history:
Submission date: 25 February 2026
Acceptance date: 25 June 2026
Publication date: 27 August 2026

Check for updates

*Correspondence:
AG: andreas.grois@unibw.de

Peer review:
Single blind

Keywords:
interaction; ducts; intake and compressor interaction; flow distortion; highly bent intakes

Citation:
Grois A., Oberthür L., Scheibel J., Stößel M., Dragan K., and Krummenauer M. (2026). Dynamic flow distortions in a highly bent engine intake: A comparative analysis of compressor influence on flow distortion characteristic. Journal of the Global Power and Propulsion Society. 10: 138–154.
https://doi.org/10.33737/jgpps/225034

Andreas Grois[1,*], Luis Oberthür[1], Julian Scheibel[1], Marcel Stößel[1], Kozulovic Dragan[1], Michael Krummenauer[2]

[1]*Institute of Jet Propulsion, Department of Aerospace Engineering, University of the Bundeswehr Munich, Werner-Heisenberg-Weg 39, Neubiberg D-85577, Germany*
[2]*Bundeswehr Technical Centre for Aircraft and Aeronautical Equipment (WTD 61), Flugplatz, Manching 85077, Germany*

Abstract

The role of unmanned aerial systems (UAS) is becoming increasingly important in aerospace development across a range of disciplines. The integration of complete engines into aircraft fuselages, along with highly curved intake ducts, offers significant advantages due to their compact size and minimal impact on structural weight. A compact intake design can lead to substantial flow distortions and negatively affect the performance and flow stability of the engine. Today's industry practice for flow distortion quantification in propulsion system integration relies on isolated pressure measurements at the engine front. Recent studies have shown that this low-accuracy approach is not adequate to complex future aircraft designs, as these assessment methods cannot capture pertinent features of flow distortion. Traditional distortion descriptors like the DC_{60} can provide a simplified total pressure distortion based on a 60-degree weighted angular section. More complex distortion patterns beyond the coverage of these sections are underrated. The phenomena arising from the instability of secondary flows cannot be captured adequately by traditional descriptors. Frequencies associated with certain flow distortion phenomena significantly affect the engine fan's response. This study uses additional newly defined flow distortion descriptors to close these gaps, such as the area integral of the secondary kinetic energy or the resulting load of the wall pressure distribution at the aerodynamic interface plane. Using the coefficient for the secondary vorticity also makes it possible to identify the dominant frequencies of the vortex systems that occur in the coupled intake system and affect the engine. The coupling shifts the first mode of the central flow separation from 15.7 to 25.1 Hz and introduces a new 75.2 Hz mode. A dominant 150.4 Hz mode, close to the measured 153 Hz is also found. The results demonstrate that advanced, time-resolved distortion metrics enable an effective analysis of intake–compressor interaction and are therefore essential for evaluating highly integrated propulsion systems.

Introduction

Unmanned Aerial Systems (UAS) are attracting significant attention in aerospace research and development as a result of their wide range of applications in various aerospace fields (Chahl, 2015). In military applications, efforts are being made to fully integrate propulsion systems into the aircraft fuselage (Johansson, 2006). Highly bent intakes offer significant advantages because their small size allows close integration into the fuselage, while also reducing structural weight and preventing radar reflections from the fan. Using complex, S-shaped intake systems with strong curvature, however, presents a challenge in terms of total pressure and swirl distortion, resulting in reduced engine performance and stability limitations (Rademakers et al., 2016; Migliorini et al., 2023). Callahan and Stenning (1971) investigated the effects of a compressor system on static pressure distortions caused by a screen in the inflow. Other studies have shown that the total pressure distortion are relatively constant when influenced by the compressor (Soeder and Bobula, 1979). The impact of steady-state flow distortion gained significant focus over the years (Haug and Niehuis, 2017; Haug et al., 2018; Maghsoudi et al., 2020). Transient total pressure distortion in intake systems was first found to be critical to aircraft engine performance early in fighter aircraft engine development. The study identified engine stall as a potential result of time-dependent distortion (Bowditch and Coltrin, 1983). Challenges that emerged in the development cycle of a series of aircraft led to significant efforts to characterize such intake flows and understand engine response. Flow distortions can arise from a wide range of aerodynamic effects, such as boundary layer ingestion or secondary internal flows. General aircraft intakes and S-shaped ducts in the context of flow distortion quantification has been investigated in a wide range of research. Previous studies demonstrated that total pressure distortion with the interacting counter-rotating vortex systems significantly reduces the surge margin and stability of the engine (SAE International, 2022). Local maxima of parameters to quantify the flow distortions had a significant effect on the engine (Stevens et al., 1978). Unsteady distortion analysis revealed that peak radial and circumferential distortions were not synchronous, requiring both to be evaluated (Tanguy et al., 2018). Migliorini et al. (2024) showed that flow separation at the second bend of the S-shaped diffuser significantly affects the swirl distortion and exhibits strong low-frequency oscillations, which are tied to the shedding of secondary flow structures. The Society of Automotive Engineers (SAE) developed a series of indices to quantify the effects of total pressure loss and the flow distortion pattern at the Aerodynamic Interface Plane (AIP) (SAE International, 2017). The presence of highly unsteady flows in complex S-ducts (Berens et al., 2014) and the importance of dynamic distortion on the fan response (Bowditch and Coltrin, 1983) have challenged the limitations of conventional flow distortion determination methods. Furthermore, a study showed that approaches based on stationary Reynolds Averaged Navier Stokes (RANS) simulation models ignore necessary aerodynamic effects (Fiola and Agarwal, 2015). It is difficult to accurately predict the onset and extent of flow separation, especially in areas with high pressure gradients and strong curvature. A study by Piovesan et al. (2024) showed that current turbulence models may have limitations in accurately capturing unsteady flow features when analyzing unsteady aerodynamic behavior in S-ducts.

In this study, high-resolution Unsteady (U)RANS simulations, based on experimental studies (Rademakers et al., 2024) are carried out. A comprehensive simulation model combining the Low Pressure Compressor (LPC) and the intake system reveals the LPC's steady-state and unsteady influence on the intake. Advanced distortion descriptors in combination with standard SAE parameters enable the analysis of complex phenomena. The main contributions of this work are:

- Introduction of physically motivated distortion descriptors capable of resolving secondary-flow-driven unsteadiness.
- Quantification of modal frequency shifts caused by LPC upstream interaction.
- Demonstration of limitations of DC_{60}/SC_{60} for dynamic distortion assessment.
- Analysis of axial-position effects between DOP and AIP.

Methodology

Intake and engine model

The model used for the numerical investigations consists of the highly bent intake duct Military Engine Intake Research Duct (MEIRD) and the jet engine Larzac 04 C5. It focuses on analyzing flow distortions and the interaction with the engine's LPC. The engine's robust design and its unmixed nozzle enable extensive throttling of the LPC (Rademakers et al., 2024). It is a turbofan engine with core and bypass mass flow divided downstream of the LPC. The LPC has two stages (R1 [x23], S1 [x61] and R2 [x29], S2 [x43]) with a tandem stator (S2) in the second stage (Figure 1). Both rotor stages are in a fully subsonic relative flow regime up to a relative spool speed of $n_{\mathrm{red,rel}} = 81\%$. Technical data of the Larzac engine and a comprehensive performance analysis can be found in Scheibel et al. (2024) and Stößel (2017).

The compact intake duct design offers flexibility for integrity aircraft and intake systems requiring more space for cargo or technical equipment, such as UAS. The highly bent MEIRD is a test case for academic research. A

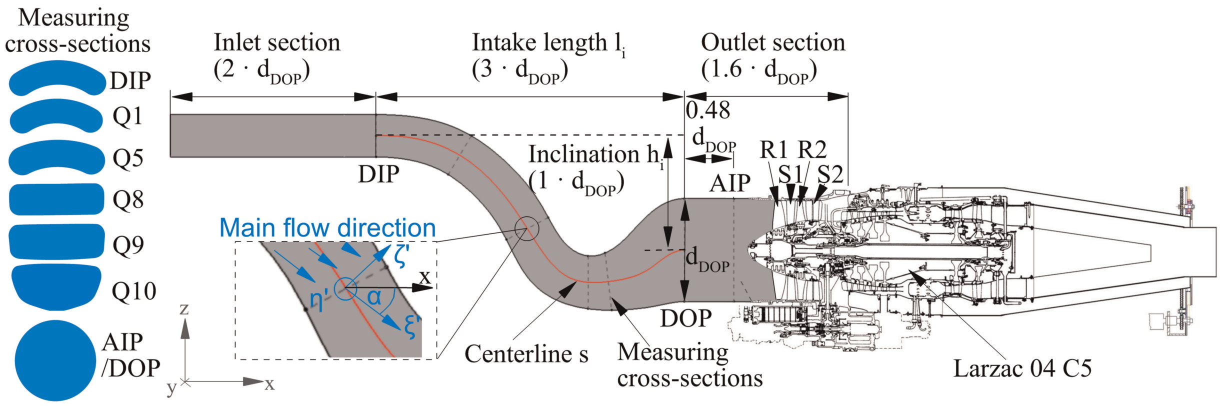

Figure 1. Scheme of the coupled configuration of MEIRD and Larzac 04 C5.

real flight application is not desirable with this design. Rather, extreme flow behavior can be investigated. The MEIRD has an outlet diameter of $d_{\text{DOP}} = 0.454$ m (Duct Outlet Plane (DOP)) and an axial length of $3 \cdot d_{\text{DOP}}$, with the AIP located $0.48 \cdot d_{\text{DOP}}$ downstream of the DOP (Figure 1). The duct features an outlet area (DOP) to inlet area ratio (Duct Inlet Plane (DIP)) ($A_{\text{DOP}}/A_{\text{DIP}}$) of 1.17. The inlet ($2 \cdot d_{\text{DOP}}$) and outlet sections ($1.6 \cdot d_{\text{DOP}}$) specify the extent of the numerical domain. In the coupled setup, the LPC is located at the rear of the outlet section. The intake system is defined by a global coordinate system (x, y, z) and an additional local coordinate system (blue, ξ, η, ζ) at the respective cross-sections (Q), which is aligned with the local main flow direction. This enables an advanced determination of more complex distortion descriptors in the later analysis. Due to the double S-shape, there is no direct line of sight from the DIP to the DOP to prevent radar-reflections from the LPC. The cross-sections change from a kidney shape at the DIP to a square at the lowest position (Q8) and back to a round shape at the DOP (Figure 1).

A pair of Lateral Vortices (LV) forms near cross-section Q5, which arise from the low-energy fluid from the thickening boundary layer and the kidney shape at the inlet. The flow, accelerated by the strong curvature near cross-section Q8, causes strong pressure gradients and a strong central flow separation (Flow Separation Bubble (SB)). The result is a complex interacting vortex system, causing strong flow distortions and separations, negatively affecting the engine's performance. A comprehensive flow analysis along with phenomenological descriptions can be found in the work of Hanrahan et al. (2025) and Grois et al. (2023, 2024).

Numerical modeling

In this study, steady-state and unsteady RANS Computational Fluid Dynamic (CFD) simulations were performed to predict the flow of a fully coupled intake and LPC system and an isolated intake model. The steady-state simulations are used as the initial solution for the unsteady simulations and as stationary comparative data for the results. The simulations were carried out using ANSYS CFX with Menter's k-ω-SST turbulence model (fully turbulent flow) with the additional option of curvature correction to reduce two-equation model problems with streamline curvature (Spalart-Shur) (Smirnov and Menter, 2009). Previous studies have shown the capability of calculating non-uniform duct flows with these modelling approaches (Brehm et al., 2014). A high-resolution second-order scheme was used to discretize the advection term, and a second-order backward Euler scheme was used to solve the transient terms. The inlet conditions were defined by p_t and T_t. The S2 outlet was described by the Exit Corrected Mass Flow (ECMF). Due to the asymmetric intake flow distortion propagated through the LPC stages, pressure outlet conditions with radial equilibrium or averaging over the entire outlet have proven to be more unstable over extremely long periods in unsteady simulations. Both Mixing Plane (MP) and Frozen Rotor (FR) interfaces (intake to spinner, spinner to R1, R1 to S1, S1 to R2, R2 to S2) were selected for the steady-state simulation. Transient interfaces were chosen for the unsteady simulation to fully capture the upstream effect of the LPC. The operating point investigated corresponds to a relative spool speed of $n_{\text{red,rel}} = 76\%$ ($\simeq$13,667 RPM) in a subsonic flow regime on the test bench under ambient conditions ($T_{t,\text{In}} = 303.15$ K and $p_{t,\text{In}} = 94{,}217$ Pa). The unsteady simulation's time step was defined as 1° of the LPC rotation ($\Delta t = 1.22 \cdot 10^{-5}$ s). This also allowed adequate convergence (momentum and mass residual (RMS) value $\leq 1 \cdot 10^{-5}$) to be achieved with reasonable computational costs (max. at 25 inner loop iter., criterion usually fulfilled after 6–10 iter.), while also covering the sampling rate required for later analysis and the modes occurring in the duct flow. The investigation of unsteady phenomena of the LPC flow is not part of the work and would require a smaller time step. The simulations cover a total of 100 LPC rotations.

The selected blade's geometry is based on a former fluid-structure interaction (FSI) steady-state RANS simulation with ANSYS CFX to determine the LPC's performance shift (Scheibel et al., 2022). The meshes used in this study are based on the resulting geometries. The results provided information on the stationary deformation of R1 and R2 as a function of the spool speed and throttle state. It showed a maximum deformation of 3.82 mm and a tip stagger angle change of 0.4° at a relative spool speed of $n_{\mathrm{red,rel}} = 76\%$, significantly affecting the LPC's performance. The dynamic influence of the FSI was neglected.

Meshing and convergence control

The block-structured meshes for the intake and the spinner were generated using ANSYS ICEM with a central H-block and an outer O-grid for wall resolution. The LPC's blade mesh was generated by ANSYS TurboGrid. The wall refinement allows a low Reynolds number treatment and a dimensionless wall distance of $y^+ \leq 1$. The mesh-independence study focuses on the influence of the LPC on the intake. Therefore, different LPC meshes were evaluated. Mesh studies already exist for the MEIRD. In an initial mesh convergence study of the isolated intake, a mesh element number of 4 million was found to be adequate for flow prediction (Haug and Niehuis, 2017). More recent studies with a focus on detailed turbulence modeling required higher mesh element numbers (Hanrahan et al., 2025). Therefore, high-resolution intake and spinner mesh with 23.2 million and 7.6 million mesh elements will be used without change (L1, M1, H1, H2) for the mesh convergence study done in this work. For analyzing the influence of coupled intake and LPC, mesh M2 uses a coarser intake mesh with 4.2 Mio and a spinner mesh with 1.9 Mio mesh elements. The simulation domain consists of the full annulus LPC. The LPC's mesh element size is changed globally (total mesh elements, Mio.: L1: 91.2, M1: 137.7, M2: 113.0, H1: 210.8, H2: 270.2).

The mesh convergence study is based on the steady-state simulations. Additional convergence criteria for monitoring the area averaged pressure ($\overline{p}_{\mathrm{AIP|S2Out}}$) and mass flow ($\dot{m}_{\mathrm{AIP|S2Out}}$) fluctuation at AIP and the S2 outlet were defined (Figure 2, left). Mean square residuals (RMS) were obtained at AIP (Figure 2, right). A total of 10,000 iterations were run for the study; Figure 2 show a sample of 7,000 iterations. The global convergence criterion was set to $1 \cdot 10^{-5}$. The convergence criterion for normalized pressure and mass flow fluctuations was 0.0005. A FR and a MP with the H1 mesh were also investigated to see the effect of asymmetric flow distortions or the radial averaging of the intake flow to the steady-state LPC. The meshes M1, H1/MP, and H2 have only a minor impact on pressure and mass flow fluctuations at the AIP and the S2 outlet. The H1/FR mesh shows a lower ($\dot{m}_{\mathrm{AIP|S2Out}}$) and a higher ($\overline{p}_{\mathrm{AIP|S2Out}}$) at the AIP and the S2 outlet. The coarsest mesh L1 shows only deviations with the pressures. The M2 mesh with low-resolution intake and spinner mesh shows a large pressure difference at the AIP. The H2 and H1/MP meshes show well-converging characteristics after 1,850 iterations, and mesh H1 was finally chosen. The isolated MEIRD configuration with the 23.2 million mesh reached the convergence criteria more quickly. Continued and not fully converging pressure fluctuations are caused by the highly unsteady flow behavior of the MEIRD. This is acceptable, as the convective flows between duct and LPC under the influence of flow distortions are crucial for the coupled setup. The results of the steady-state mesh convergence study are applied to the URANS mesh and simulations.

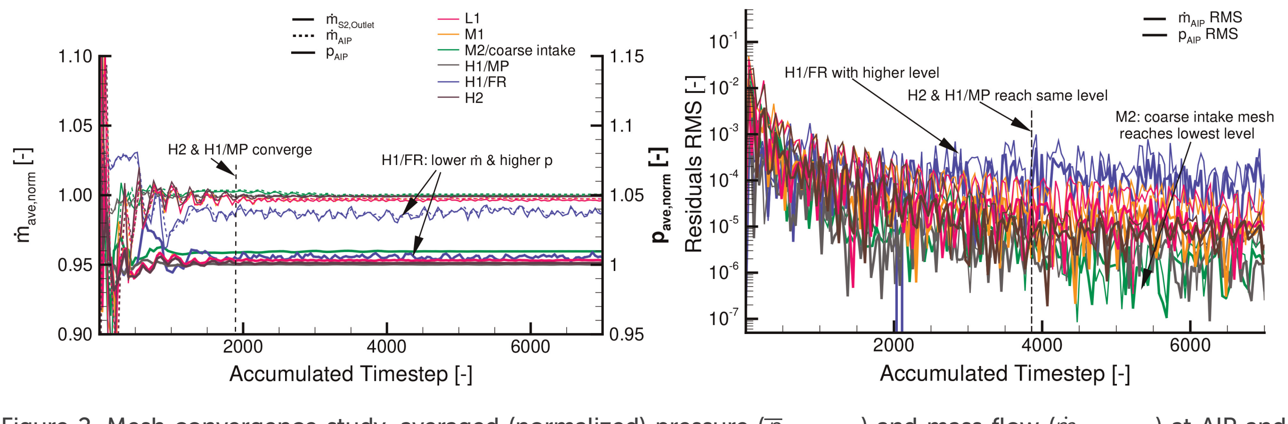

Figure 2. Mesh convergence study, averaged (normalized) pressure ($\overline{p}_{\mathrm{AIP|S2Out}}$) and mass flow ($\dot{m}_{\mathrm{AIP|S2Out}}$) at AIP and the S2 outlet (left), RMS residuals at the AIP (right).

Validation of the numerical model

The wall pressures resulting from the simulations are compared with experimental data from a previous study of the coupled MEIRD and Larzac 04 C5 engine (Rademakers et al., 2024). Figure 3 shows the Pressure Recovery (PR) ($p/p_{t,\mathrm{DIP}}$) related to the inlet conditions and a scheme of the MEIRD with the named cross-sections. In addition, the results are compared with an existing and well-known setup using the DLR's flow solver TRACE and the Hellsten explicit algebraic Reynolds stress (EARSM) turbulence model (blue), *(2)* (*MEIRD only, DLR's TRACE w. EARSM*) (Grois et al., 2023). *(2)* shows a good correlation with the exp. wall pressures. Differences are observed in the central flow separation (SB) region. More significant differences are shown by simulations *(3) (MEIRD only, CFX w. SST-k-ω)*, *(4) (MEIRD and Larzac 04 C5, CFX w. SST-k-ω, MP)*, *(5) (MEIRD and Larzac 04 C5, CFX w. SST-k-ω, unsteady, 7th LPC rev.)*, which rely on CFX and *k-ω-SST* turbulence model.

Near (A), a deviation to the experimental data is given by the isolated MEIRD simulation (*3*), which does not occur in the coupled simulations *(4)* and *(5)*. The coupled CFD and TRACE simulations similarly predict the lowest peak (B). The positioning of the interface between the spinner and the intake (IF) results in a discontinuity of the wall pressures. Finally, the CFD models show a good correlation with the experimental data. Areas of strong flow separation are not accurately reproduced but modeled qualitatively. Further detailed num. and exp. wall pressure data can be found in (Hanrahan et al., 2025).

Distortion descriptors

The distortion descriptors quantitatively describe the flow inhomogeneity on the engine and intake interfaces. The parameters have been determined at the cross-sections marked in Figure 1 (see also (Grois et al., 2024)) as surface integrals ($_A$) or as integrated circumferential ($_b$) pressure value (see Figure 4). In this paper, parameters at the DOP and AIP are considered. In addition to traditional distortion descriptors, such as DC_{60} und SC_{60} (SAE International, 2011), advanced parameters are also discussed. The additional parameters react differently to various aerodynamic phenomena and offer significant advantages compared to traditional turbomachinery parameters (Grois et al., 2023). Coefficients are used to correlate the values.

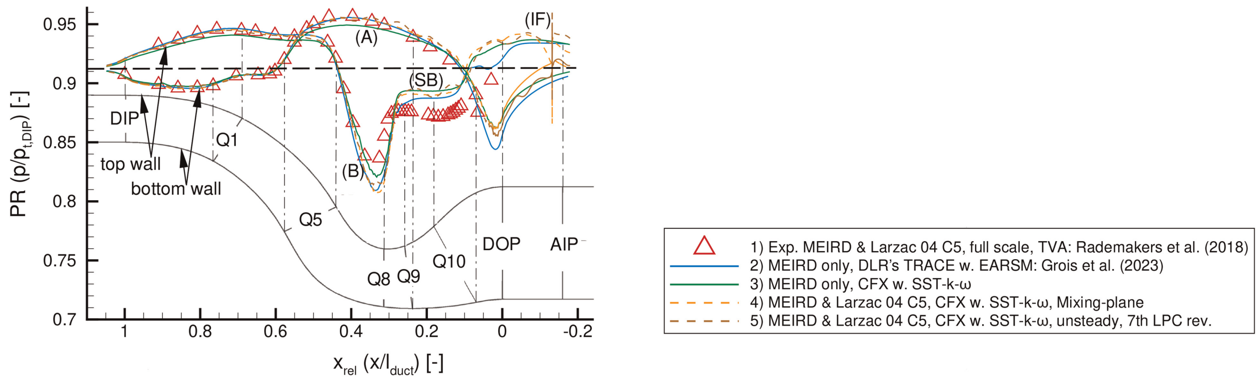

Figure 3. Wall pressure profile of the MEIRD, comparison of exp. (Rademakers et al., 2018) and num. data, isolated intake vs. coupled intake and engine.

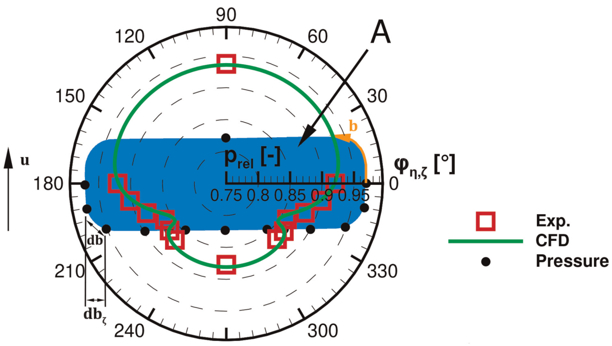

Figure 4. Determination of the cross-sectional flow inhomogeneity parameters, example: cross-section Q8.

Integrating the wall pressure profile at the cross-section gives the load vector $L_{s,\xi}$ (Equation 1). The load represents the aerodynamic lift exerted on the perimeter of the cross-section. More inhomogeneous flow will result in higher load and greater pressure losses, indicating that this is an appropriate parameter (Grois et al., 2023, 2024). The coefficient is calculated using the maximum load occurring in the duct flow.

$$c_{L,s,\xi} = \frac{L_{s,\xi}}{\max_i (L_{s,\xi})} \quad \text{with } L_{s,\xi} = \oint_0^B p(b)\, \mathrm{d}b_\xi \tag{1}$$

The parameter for the distorted mass flow ratio μ_{di} is defined by the separation of the sectional areas into clean ($_{\mathrm{cl}}$) and distorted ($_{\mathrm{di}}$) fractions (Equation 2) (Figure 5). The limiter for the splitting is the area averaged total pressure $\overline{p}_{t,Q}$ at the cross-sections minus a half of the intake pressure loss $\Delta p_{t,i}$. This approach has proven to be the most versatile. As a result, the parameter identifies changes in the flow behavior along the intake flow ($\mu_{\Upsilon,di}$) (Equation 2).

$$\mu_{di} = \frac{\dot{m}_{di}}{\dot{m}_{cl}} \quad \text{with } \dot{m}_i = \begin{cases} \dot{m}_{di} & \text{if } p_t < p_{t,limit} \\ \dot{m}_{\mathrm{cl}} & \text{if } p_t \geq p_{t,limit} \end{cases} \quad \text{for } \mu_{\Upsilon,di}: \quad p_{t,limit} = \overline{p}_{t,Q} - \frac{1}{2}\Delta \overline{p}_{t,i} \tag{2}$$

The area integral of the secondary kinetic energy Secondary Kinetic Energy (SKE) (Equation 3) is based on the velocity components perpendicular to the main flow direction and aligned with the blue ξ, η, ζ coordinate system. Secondary flow occurs in regions where the forces acting on a fluid element tend to deflect that fluid element from the primary direction, which, in this case, is mostly aligned with the centerline of the duct. The generated vortex systems cause a partial transformation of kinetic energy into SKE (Nikitin et al., 2021). Therefore, the SKE indicates flow losses and identifies areas of flow interaction, e.g. between vortices (Figure 5). The coefficient $c_{\mathrm{SKE},A}$ is defined using $(\frac{1}{2}\rho v^2)_{\mathrm{DIP}}$ at the DIP to show the rise with the duct flow.

$$c_{SKE,A} = \frac{SKE_A}{\left(\frac{1}{2}\rho v^2\right)_{DIP} \cdot A} \quad \text{with } SKE_A = \int_A \frac{1}{2}\rho\left(v_{\zeta'}^2 + v_{\eta'}^2\right) dA \tag{3}$$

The vorticity ω is a principal parameter obtained from the velocity field that indicates the presence of vortical structures. It uniquely identifies the dimensions of the vortex and its core. In addition, the secondary vorticity ω_{sec} includes flow components that are perpendicular to the main flow direction and can be used as an additional indicator of longitudinal vortices (Equation 4). Positive and negative signs allow the differentiation of flow regions into right- and left-spinning parts, as shown in the colored Figure 5 (right). The classification by region (SI, SII, SIII) enables information to be obtained from certain phenomena that occur in the flow of the MEIRD. The coefficient $c_{\omega,\mathrm{sec},A}$ is formed by the vorticity magnitude along the duct flow to show the secondary part in relation.

$$c_{\omega,sec,A} = \frac{\omega_{\mathrm{sec},A}}{|\omega|_i \cdot A} \quad \text{with } \omega_{sec,A} = \int_A \left(\frac{\partial v_{\zeta'}}{\partial \eta'} - \frac{\partial v_{\eta'}}{\partial \zeta'}\right) dA \tag{4}$$

The distortion coefficient DC_{60} (Equation 5) specifies the total pressure distortion for a certain cross-section in a fixed angular range of 60 degrees. This allows the intensity of the flow non-uniformity to be determined.

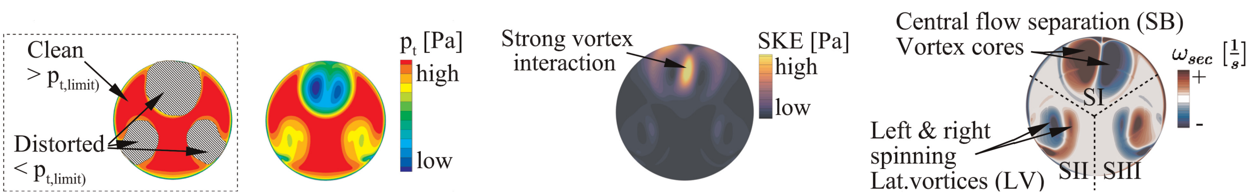

Figure 5. Total pressure p_t plot with clean (cl) and distorted (di) split (left) and advanced distortion descriptors SKE (middle) and ω_{sec} (right) (area sectioning: SI - central flow separation (SB), SII and SIII - lateral vortices (LV)), (DOP).

The method is based on SAE standards and uses pressure transducers on the cross-section (SAE International, 2011, 2017).

$$\mathrm{DC}_{60} = \max\left(\frac{\bar{p}_{t,Q} - \bar{p}_{t,60}}{\bar{q}_Q}\right) \tag{5}$$

The swirl coefficient SC_{60} (Equation 6) is defined by an analogous angular sector. It is determined by the ratio of the mean circumferential speed $v_{\varphi_{\eta',\zeta'},\max,60}$ to the mean axial speed v_Q. φ is the circumferential coordinate of the polar diagram of the cross-sections.

$$\mathrm{SC}_{60} = \max\left(\frac{\left|v_{\varphi_{\eta',\zeta'},\max,60}\right|}{\left|\bar{v}_Q\right|}\right) \tag{6}$$

Unsteady post-processing

The post-processing is designed to determine advanced distortion coefficients to quantify the unsteady intake compressor interaction. Given the computing time required, the time-consuming CFD simulation and the resulting data are post-processed in parallel (Figure 6). The boundary conditions for the CFD are derived from the test bench conditions of the experiments used for the validation. The steady-state CFD serves as an initial solution for the transient simulation. Unsteady CFD results are exported for each third of a single LPC rotation. This corresponds to a time step of $1.464 \cdot 10^{-3}$ s and a nominal sampling rate of 683 Hz for the parameter's temporal signal capture. The maximum expected dominant intake flow frequency is $f_{\max,\mathrm{intake}} = 193\,\mathrm{Hz}$, which was experimentally determined (Rademakers et al., 2024). Phenomena with frequencies up to the LPC rotation ($f_{lpc,N76} = 227\,\mathrm{Hz}$) must be considered. One study also detected phenomena with a frequency range of 250–450 Hz in the center of the AIP (Tanguy et al., 2018). The Nyquist-Shannon theorem specifies a sampling rate twice that of the output signal to be fully determined (Granot, 2019). In post-processing step (1), the exported time step data are analyzed with pyTecplot. The distortion descriptors are calculated and recorded. The determined parameters are used to create contour plots of AIP and DOP. In the post-processing step (2), the specific distortion parameters are read in a temporal series. The data is analyzed for a limited time-period. Due to the small amount of temporal data available, the signal is resampled using the Fourier method (Laird et al., 2004). Dominant frequencies of the resulting temporal signal of each distortion parameter are quantified using Power Spectral Density (PSD) analysis. The estimation is based on the periodogram method, a function of the fast Fourier transformation. Studies have shown that URANS simulation with PSD analysis can provide results similar to experiments and scale-resolved simulation (Liu et al., 2024). Frequencies are given as the Strouhal number *St* (Equation 7), which is well suited for comparing the obtained results with data from the literature. Studies also showed that a simple bent pipe for analyzing transient flow phenomena is mostly at lower Reynolds numbers, below 10^6 (Rademakers et al., 2024), which can be transferred to the basic duct flow. Typically, the unsteadiness of secondary flow phenomena, such as shear layer instabilities, or vortex switching and local vortex shedding occurs between $0.1 < \mathrm{St} < 0.4$ (Rütten et al., 2005). Recent experimental studies by Garnier found dominant total pressure fluctuations ($0.25 \leq \mathrm{St} \leq 0.625$) caused by secondary flows downstream of an s-duct (Garnier, 2015).

$$\mathrm{St} = \frac{f \cdot d_{\mathrm{DOP}}}{v_{\mathrm{DOP}}} \tag{7}$$

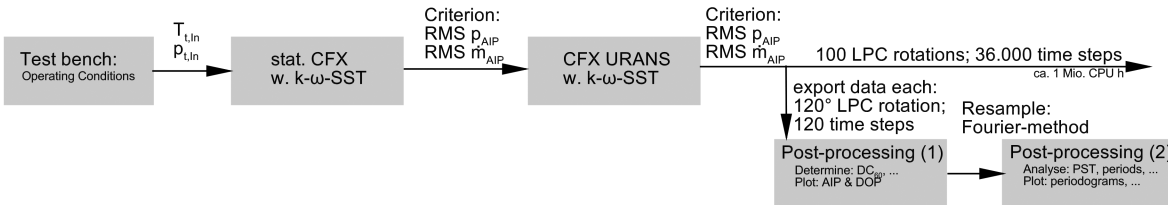

Figure 6. Post-processing chain, unsteady intake and LPC interaction distortion descriptors analysis.

Results

General flow behavior

The analysis of the general flow behavior and the vortex systems helps to understand the aerodynamics of the intake system (Figure 7). The duct flow is characterized by two dominant phenomena: the lateral vortices LV and the large central flow separation SB, which are discussed in this paper and analyzed in terms of their frequency modes.

In the area near cross-section Q5, early flow separation occurs due to the inflow of low-energy fluid. This leads to the formation of the lateral vortex pair LV, which is caused by the thick boundary layer and the kidney-shaped inlet geometry. The flow, accelerated by the strong curvature near cross-section Q8, causes strong pressure gradients and a large central flow separation (SB). The intake design prevents further deceleration of the flow. The main distortion pattern is driven by the large central flow separation SB. At the DOP, different phenomena result in a highly interacting system, capturing diverse modal frequencies, as shown in the following unsteady analysis. Near region SB*, the SB expands and shapes around the spinner, following the direction of LPC's rotation. A comprehensive flow analysis along with phenomenological descriptions can be found in the work of Hanrahan et al. (2025) and Grois et al. (2023, 2024).

Flow distortion pattern

The flow distortions are classified by the different distortion descriptors at the DOP for specific time steps (Figure 8, Table 1). This allows certain states of flow distortion to be shown using descriptors with different sensitivities, which helps one to understand the later frequency analysis in this study. The time steps show key aspects of the periods with significant phenomena. The contour plots compare one time step for the isolated intake (left column, C0) with four time steps of the coupled intake and LPC configuration (right columns, C1, C2, C3, C4). The later analysis will show that the vortex structures of the isolated intake change minimally over time (Section "Isolated intake"), meaning that only a single time step of the isolated intake is shown and used as a basis for comparison.

The dominant flow phenomena LV and SB are displayed for isolated intake (C0). In the middle section of the SB, there is a peak in SKE, indicating strong interaction between the vortices (middle row). Regions SI, SII, and SIII show the clear split and position of the right- and left-turning flow components of the vortices (bottom row).

A comparison with the same time ($t = 0.0254$ s, C1) reveals a similar distortion pattern for the coupled intake and LPC configuration. The asymmetry Ⓐ points in the opposite direction (compared to C0) toward the LPC rotation. In the center of the DOP Ⓑ, an upstream effect of the spinner caused by a local change in *PR* is observed. The SKE shows a local increase in region Ⓗ compared to the isolated intake. The central pair of small vortices above the SB (Ⓜ) shows a reverse direction of rotation compared to C0 (ω_{sec} colors switched). Therefore,

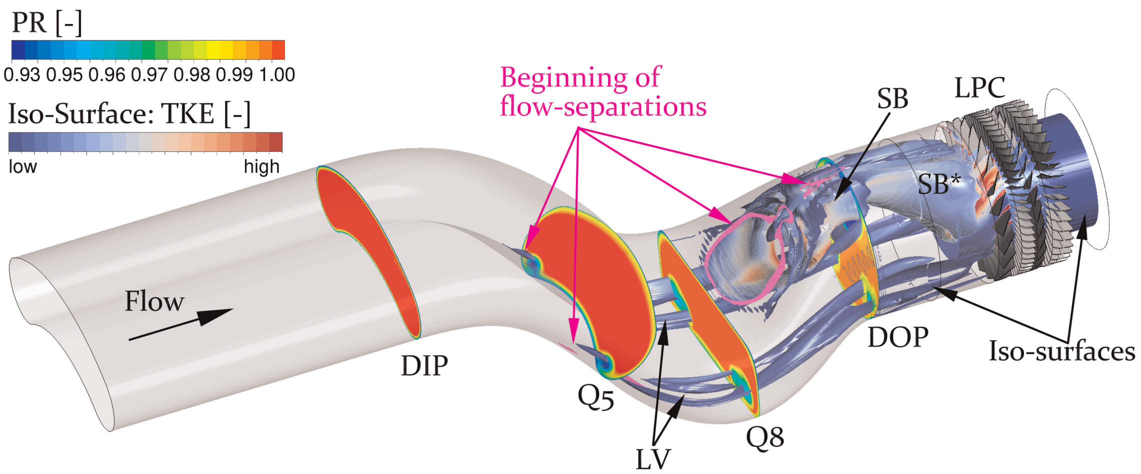

Figure 7. Flow behavior and vortex systems of the MEIRD, cross-sections Qx with $\mathrm{PR} = p_t/p_{t,\mathrm{DIP}}$, Q-criterion, and radial iso-surfaces with colored TKE.

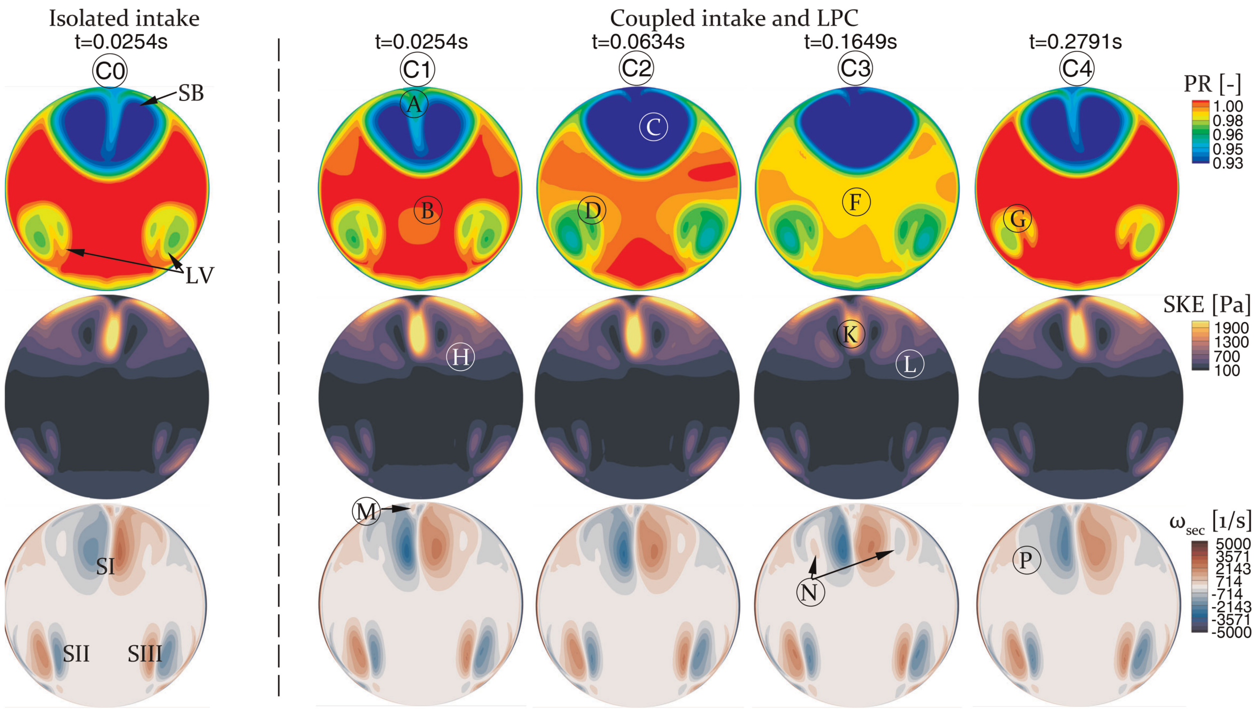

Figure 8. Flow distortion pattern (PR (top), SKE (middle), ω_{sec} (bottom)) at the DOP for different time steps, comparison of one time step of the isolated intake and four time steps of the coupled intake and LPC.

Table 1. Flow distortion descriptors, discrete values for specific time steps and LPC revolutions, comparison of one time step of the isolated intake (Iso. int.) and four time steps of the coupled intake and LPC (Cpld.).

		Iso. int.	Cpld.			
t	[s]	0.0254	0.0254	0.0634	0.1649	0.2791
rev	[-]	(5.8)	5.8	14.4	37.6	63.5
$c_{\omega,\text{sec},A}$	[-]	0.058	0.063	0.062	0.058	0.061
$c_{L,s,\xi}$	[-]	0.089	0.080	0.078	0.073	0.076
$c_{\text{SKE},A}$	[-]	0.138	0.135	0.133	0.111	0.121
$\mu_{\Upsilon,\text{di}}$	[-]	0.276	0.274	0.257	0.185	0.315
DC_{60}	[-]	0.662	0.579	0.697	0.648	0.696
SC_{60}	[-]	0.259	0.277	0.255	0.263	0.254

the DC_{60} is 12.5% smaller at 0.579 (Table 1) compared to the isolated intake. The $c_{\text{SKE},A}$ remains almost unchanged, which highlights the observations. $c_{\omega,\text{sec},A}$ increases from 0.058 to 0.063.

As time progresses ($t = 0.0634$ s, C2), a change in total pressure distortion pattern emerges. The SB is becoming larger (C). The LV's area of influence is larger, so the region with lower PR is wider C. A change in the distribution of SKE and ω_{sec} at the DOP is minor for C2 compared to C1. The discrete values for $t = 0.0634$ s show, only an increase in DC_{60} compared to $t = 0.0254$ s (Table 1). This is due to the 60° weighted section, which detects the increase due to the local PR drop of the SB.

At $t = 0.1649$ s (C3), no further change in the SB can be observed in means of the PR distribution. A global drop in PR occurs in regions around the vortices at the DOP (Ⓕ, orange contours). The region of interaction of the SB vortex cores is smaller in terms of *SKE* (Ⓚ). In area Ⓛ, in the middle of the left and right vortex cores of the SB, a local rise in the SKE forms, indicating a splitting of these cores. The ω_{sec} shows this splitting phenomenon with two additional counter-rotating pairs of vortices Ⓝ. In terms of the discrete values, the reduction in SKE at interaction region Ⓚ leads to a significantly lower $c_{\mathrm{SKE},A}$ of 0.111 compared to the other time steps (Table 1). The ratio of distorted mass flow $\mu_{\Upsilon,\mathrm{di}}$ decreased by 32% compared to C1, indicating a substantial reduction in flow non-uniformity.

The distortion pattern at C4 resembles that of C1, with 16.8% variation in DC_{60}, and similar flow topology. The drop in PR is limited to the regions of the SB and the LV. However, the LV's area of influence is smaller (Ⓖ). The SB shows a clear and closed shape (Ⓟ), with no signs of splitting. The ratio of distorted mass flow $\mu_{\Upsilon,\mathrm{di}}$ is highest at 0.315 compared to the other time steps (Table 1).

Isolated intake

The frequency analysis of the isolated intake enables the identification of isolated flow phenomena. The analysis of the temporal signal characteristics of the flow distortion parameters refers to the DOP. The influences of the compressor are excluded. The vorticity ω is a quantity related to rotation of the velocity field of the flow in the duct, and is highly sensitive to the dominant frequencies of mainly longitudinal vortex systems. Figure 9 shows the PSD analysis of $c_{\omega,\mathrm{sec},A}$, divided into the three sub-regions SI, SII, and SIII, and into the right ($^+$) and left-spinning ($^-$) parts of the flow. The sub-areas are assigned to the locally occurring flow phenomena: lateral vortices (LV) and the large central flow separation (SB). In this way, the PSD analysis enables the division of the various modal frequencies (①, ②, and ③) of the respective phenomena. The blue lines show the entire cross-section without subdivision, for the right ($^+$) and left-spinning ($^-$) flow parts.

The central flow separation shows two dominant frequencies; ①: St = 0.06 at 15.7 Hz and ②: St = 0.64 at 166.8 Hz. These can be assigned to this flow phenomenon since only a trigger in the SI area occurs (region of the central flow separation). Three further modes are caused by the lateral vortex systems in the SII and SIII regions; ①: St: 0.31 at 81.8 Hz, ②: St = 0.47 at 119.6 Hz, and ③: St = 0.60 at 157.4 Hz. For small Strouhal numbers (St < 0.1, ① SB), the flow remains relatively steady. The low frequencies are associated with large-scale instabilities and are independent of the Reynolds number for an ideal and limited case of a sphere (Kim and Durbin, 1988). At higher Strouhal numbers (St > 0.3, ② SB, ① ② ③ LV), strong periodic vortex shedding leads to high-pressure oscillations (Silva-Leon and Cioncolini, 2019). The higher Strouhal numbers are caused by small-scale instabilities from the separation of the shear layer (Sakamoto and Haniu, 1990). This increases the risk of strong flow separation, which can potentially cause an LPC stall event. It also produces aerodynamic noise and structural vibrations in the intake duct (Xiong et al., 2019). Significant total pressure distortion at the front of the engine results in reduced engine performance. If the intake's resonance frequency matches the separation frequency, resonant amplification can occur, leading to structural damage.

Clockwise and counterclockwise flow components do not differ in their frequencies. The lateral vortex systems' right (SIII) and left (SII) sides show the same modes, so only SIII is demonstrated (Figure 9). In the experimental investigation by (Rademakers et al., 2024), the most dominant frequency of also 153 Hz was

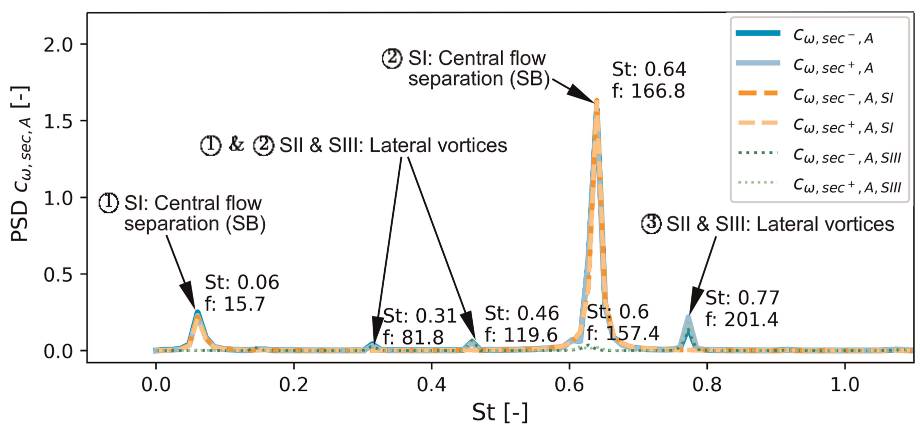

Figure 9. Spectral analysis of the subdivided flow distortion descriptor $c_{\omega,\mathrm{sec},A}$, colored lines for right and left spinning flow parts, isolated intake, f in [Hz].

recorded by four high-frequency pressure transducers mounted at different positions along the intake wall, which shows the global dominance of the associated flow phenomenon. The closest numerical frequencies are at $f = 157$ Hz, but these are slightly induced by the lateral vortices. The frequency of 166.8 Hz (② SB), which clearly dominates in the numerical results, corresponds more closely to the observations from the experiments, but is slightly shifted. However, since the influence of the LPC is absent, deviating frequencies are assumed. The third mode of the lateral vortex system is also observed in the experiment (at 193 Hz, $n_{\mathrm{red,rel}} = 76\%$) and is significantly less prominent than the mode at 153 Hz. Further frequencies are found in the range of 100 Hz, which are identified as stronger within the aft end of the duct. This corresponds to the spectral range of the first and second modes of the lateral vortex system. Previous studies have shown that these vortices interact strongly and exhibit small-scale fluctuations that URANS simulations cannot completely cover. Since the primary modes can also be detected in the isolated intake simulation, it proves the statement of Rademakers et al. (2024) that the three modes are independent of LPC rotational frequency and are mainly induced by the geometry of the intake.

The load coefficient $c_{L,s,\xi}$ is a way of measuring the flow's inhomogeneity and the intake wall's structural load. Figure 10 (left, top) shows the PSD analysis corresponding to $c_{L,s,\xi}$. No subdivision into different sections has been made. The two dominant frequencies of the central flow separation (SB) can be seen. The lateral vortex systems do not affect the temporal signal of the load. Consequently, the structural impact of the SB is expected to be the major one.

The $\mu_{\Upsilon,\mathrm{dist}}$ is highly suitable as an input for low-fidelity simulations due to the division of the flow into distorted and clean (Remiger et al., 2024). Figure 10 (middle, top) shows a volatile curve of the PSD analysis, which impedes the explicit identification of dominant frequencies. The first two frequencies of the central flow separation (SB) and lateral vortex systems (LV) are shown. The impact of ① (LV) is higher than the previous flow distortion descriptors.

The corresponding analysis of c_{SKE} shows similar results (Figure 10, right, top)). The first two dominant frequencies of the flow phenomena can be identified, with ① (LV) being indicated as the most dominant. The temporal effects of the transformation of kinetic energy into SKE through the vortex systems are strong here.

The DC_{60} enables the detection of the first two modes of the SB and the first mode of the LV. The most dominant is the ① (SB). With lower Stouhal numbers, there are less strong temporal effects on the flow inhomogeneity ($\mathrm{St} < 0.1$). This limits the usability of the DC_{60} as a dynamic flow distortion descriptor.

The SC_{60} shows similar behavior. In this case, it only detects the SB phenomena. Temporal swirl fluctuations caused by less dominant vortex systems (LV) are neglected.

A different sensitivity can be observed by comparing these flow distortion parameters for the steady-state CFD and the unsteady behavior of the URANS simulation. The steady-state load value $c_{L,s,\xi}$ is close to 0 at the DOP. This is known from previous studies (Grois et al., 2023). Here, the cross-sectional load was mainly influenced by the geometric shape of the intake, which passes zero at the outlet. Consequently, the load on the DOP is roughly steady. The evaluation of the URANS shows a deviation margin of <0.1%. The stationary value of $\mu_{\Upsilon,\mathrm{dist}}$ reaches 34.6%. The temporal signal has a span of 0.39% over minimum and maximum. The impact of the change over time is minor. The stationary c_{SKE} reaches 0.138 at the DOP. Over time, a maximum drift of 0.15% can be seen. $c_{\omega,\mathrm{sec},A}$ is defined as the ratio relative to the maximum vorticity occurring in the intake. With the DOP as a reference, a stationary value of 5.8% is obtained. As with the load, the fluctuation of the secondary

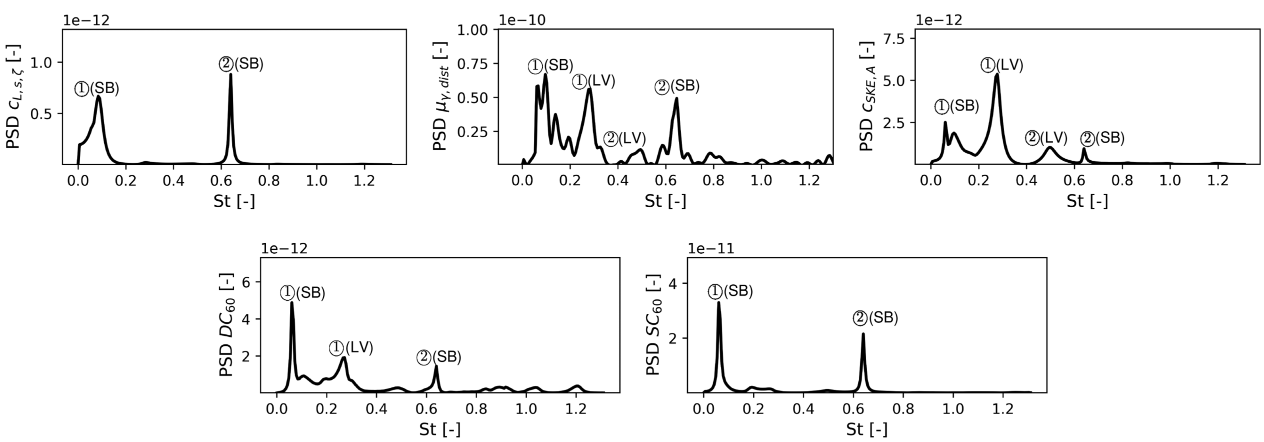

Figure 10. Spectral analysis of the distortion descriptors $c_{L,s,\xi}$ (left, top), $\mu_{\Upsilon,\mathrm{dist}}$ (middle top), c_{SKE} (right top), DC_{60} (left bottom), SC_{60} (right bottom), isolated intake.

vorticity is less than 0.1%. The DC_{60} achieves a value of 0.662 when the results of the steady-state CFD are considered. The deviation is minor with <0.1%. The stationary SC_{60} is 0.259. The time-related deviation is 0.12%.

Coupled intake and LPC

The coupled simulation results include the intake and the two-stage-LPC with spinner. The coupled approach allows conclusions to be drawn about the direct influence of the LPC on the intake flow behavior. The correlation between the Stouhal number and the frequency differs from the isolated intake observation since a slight change in the intake operating point occurs due to the coupling of the LPC. This temporal analysis of the flow distortion parameters refers to DOP.

The differences between the coupled and the isolated simulation results are evident when comparing the dominant frequencies of $c_{\omega,\mathrm{sec},A}$ (Figure 11). The first modal frequency of the large central flow separation (SB) was shifted (Modal Shift (MS) 1) from $f = 15.7$ Hz to $f = 25.1$ Hz. An additional low-frequency (St = 0.02, $f = 6.3$ Hz), which can be assigned to the lateral vortex system (SII and SIII), emerged. At $f = 75.2$ Hz, an additional dominant frequency of SB appears, which was not present in the isolated intake analysis. The large-scale domination leads to the lateral vortex system's Induced Amplification (IA) 1. The previously identified first and second modes of the lateral vortex system in the isolated intake can also be found. ① (LV) is shifted from $f = 81.8$ Hz to $f = 94.0$ Hz (MS2). The experimental results of (Rademakers et al., 2024) show in these spectral ranges (103 Hz $< f <$ 108 Hz) also a second dominant frequency, which can be assigned to the interaction of the SB (at 75.2 Hz) and LV (①: St: 0.34 at 94.0 Hz and ②: St: 0.43 at 119.1 Hz). The most dominant frequency (② (SB)) matches the value from the experiment, with $f = 150.4$ Hz of the URANS results and $f = 153$ Hz in the experiment. This modal frequency is again found to be the most dominant in CFD and experiment. The mode can be assigned to SB, but its intensity stimulates the lateral vortex system (IA2). This dominant distortion frequency corresponds to approximately 0.66 times the LPC rotational frequency (227 Hz at N76). The third mode, known from the experiments (Rademakers et al., 2024), can only be detected in its beginnings (③ (LV)). The frequency from the CFD at $f = 206.1$ Hz is close to the experimental value at $f = 193$ Hz. The overall time series of $c_{\omega,\mathrm{sec},A}$ for the coupled simulation shows a more diffuse behavior of the individual parameters (SI, SII, SIII) for identifying the vortices and flow separations. The detected frequencies of the right- and left-spinning flow components for the LV system only do not always match exactly ($^+$, $^-$), especially in the range of the induced frequency (IA1). Additional dominant frequencies have emerged and are stimulating adjoining vortex systems. A complex interplay between the diverse vortex systems' interaction and the LPC's upstream effect is evident. An excitation directly associated with the rotational frequency of the LPC was not found by the signal of $c_{\omega,\mathrm{sec},A}$. The temporal $c_{L,s,\xi}$ analysis shows minor differences when comparing the isolated intake results and the coupled results (Figure 12, left, top). The low frequency (St = 0.02, $f = 6.3$ Hz) additionally found in Figure 11 is also detected by the load coefficient. This underscores the coupling of the LPC as a trigger. $\mu_{\Upsilon,\mathrm{dist}}$ clarifies the modes found in the isolated intake. ① (SB) is less dominant. The c_{SKE} signal shows ② (SB) more dominant than in the isolated intake case. This indicates that the secondary flow losses in the central flow separation (SB) region increase due to the coupling of intake and LPC. The time-resolved DC_{60} shows a more discontinuous curve with less distinct dominant frequencies. A peak in the range of St = 0.8

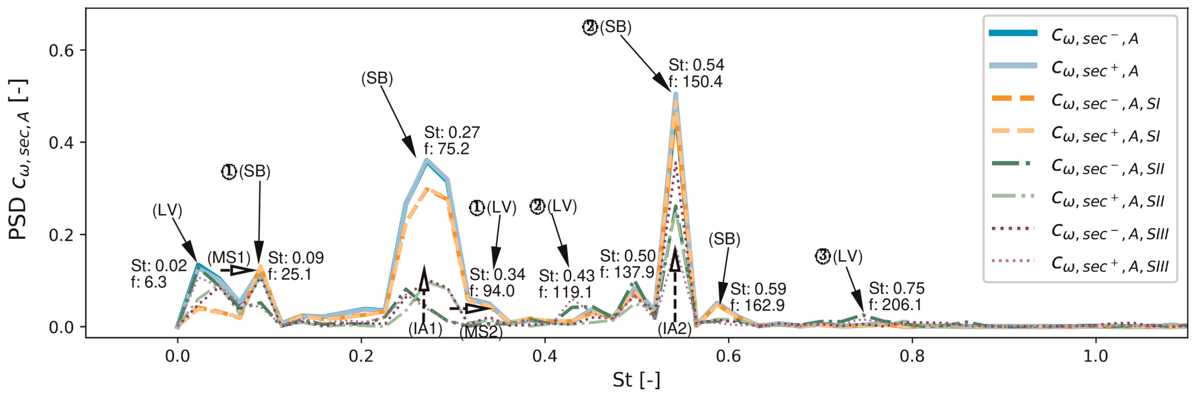

Figure 11. Spectral analysis of the flow distortion descriptor $c_{\omega,\mathrm{sec},A}$, subdivided regions, colored lines for right- and left-spinning flow parts, coupled intake and LPC, f in [Hz].

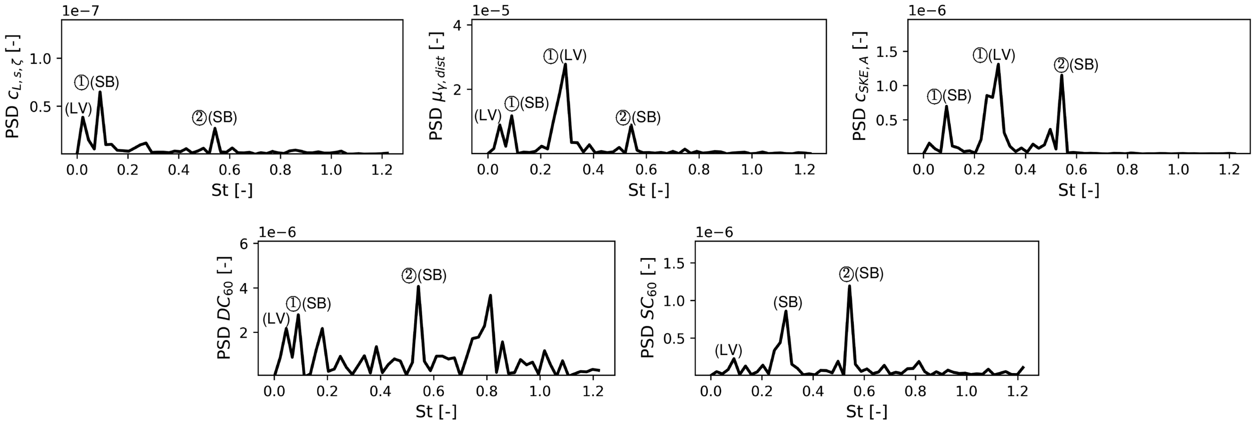

Figure 12. Spectral analysis of the distortion descriptors $c_{L,s,\xi}$ (left, top), $\mu_{\Upsilon,\mathrm{dist}}$ (middle top), c_{SKE} (right top), DC_{60} (left bottom), SC_{60} (right bottom), coupled intake and LPC.

appears, which was not found by any other parameter. Analogous to the previous parameters, the SC_{60} also shows an additional mode at $\mathrm{St} = 0.27$, which only occurs in the coupled case.

The steady-state values of the flow distortion descriptors differ only slightly between the isolated intake and the coupled case. $c_{L,s,\xi}$ is also close to 0 at the DOP. The distorted mass flow ratio $\mu_{\Upsilon,\mathrm{dist}}$ is slightly lower at 27.3% for the coupled results compared to the isolated ones. The coefficient of the secondary vortex c_{SKE} is 0.06, which is also less than the value from the isolated CFD. With 6%, $c_{\omega,\mathrm{sec},A}$ is slightly higher compared to the isolated intake value. The DC_{60}, with 0.660, does not differ. The SC_{60} is marginally larger at 0.264.

An evaluation of the deviations of the minimum and maximum values of the time signal shows more significant differences than the isolated intake results. The load showed an almost stationary behavior in the isolated intake analysis. The coupled investigation revealed deviations over time of 8.5%. The amplitudes of the $\mu_{\Upsilon,\mathrm{dist}}$ signal have a spread of more than 63% in the coupled simulation. This shows that this parameter captures the LPC's upstream effect particularly sensitively. Also, c_{SKE} with 36.4% signal spread reacts strongly to LPC influences. This is due to the increase in secondary flow losses caused by the superimposition of rotation on the flow through the LPC. The DC_{60} varies by 20.3% and reaches a maximum of 0.71. This corresponds to a very high value, which indicates a (temporary) strong total pressure distortion. Since a steady-state value usually serves as a basis for the design of the intake and engine, this illustrates the importance of analyzing unsteady fluctuations. The SC_{60} fluctuates insignificantly by 14.7% over time.

Influence of the axial position

Previous studies showed a major influence of the axial distance of the engine to the duct's aft end on the flow distortion behavior (Rademakers et al., 2024). This work analyzes two interfaces between the intake and the engine. The DOP is located directly at the outlet of the duct. The AIP is located $0.48 \cdot d_{\mathrm{DOP}}$ downstream of the DOP. This corresponds to a realistic distance in real applications. Studies have shown that the flow is already mixing between DOP and AIP, and the flow inhomogeneities are decreasing. The various flow distortion descriptors showed different behavior when the flow was mixed (Grois et al., 2023). In the following, the results of the coupled simulation are analyzed.

The time-averaged DC_{60} decreases by 18.9% downstream to the AIP. Since the spinner position is close to the AIP, an upstream effect of the spinner nose can already be observed. This leads to displacing the surrounding vortices and flow separation areas from the incoming flow. This displacement effect has a negative impact on the detection of a 60° sector by the DC_{60}, so that a strong drop occurs. $c_{L,s,\xi}$ is close to 0 at the DOP and causes a change in sign at the AIP. The surface load on the outlet channel downstream the duct can increase more than necessary if the positioning is unfavorable in aircraft design processes. On the other hand, the secondary flow losses detected by the SKE ($C_{\mathrm{SKE},A}$) decrease by 24.0%, which can positively affect the flow to the LPC blades. The ratio of the distorted mass-flow $\mu_{\Upsilon,\mathrm{dist}}$ increases by 22.4%, which has also been shown in studies (Grois et al., 2023). Like the DC_{60}, the flow distortion is described by an angular section with a drop in total pressure across the interface. This is related to the description of the distorted mass flow $\mu_{\Upsilon,\mathrm{dist}}$. However, an opposite behavior is observed here. In other words, various flow distortion descriptors must be used in the design process to consider an appropriate axial position in combination with the proper engine characteristics.

Conclusion

A highly bent engine intake's flow is characterized by specific frequencies, spatial structures, and dynamic phenomena, which can be clearly identified and quantified by an unsteady analysis and advanced flow distortion descriptors. This knowledge enables a direct causal link between intake flow distortions and their impact on engine performance and vice versa. As a result, weaknesses in intake design can be systematically identified and addressed through targeted geometric modifications or flow control strategies. This study systematically investigates advanced flow distortion descriptors to quantify unsteady intake flow phenomena and their interaction with the LPC.

The analysis of the isolated intake revealed two dominant unsteady flow phenomena

1. Lateral vortex systems (LV) in the side regions (SII, SIII) exhibit three dominant modal frequencies at 81.8, 119.6, and 157.4 Hz, corresponding to $0.31 < \mathrm{St} < 0.60$.
2. The load coefficient $c_{L,s,\xi}$ primarily captured the impact of the central flow separation (SB), indicating its significant structural relevance. Other descriptors like distorted mass flow ratio $\mu_{\Upsilon,\mathrm{dist}}$ and coefficient of the secondary kinetic energy $c_{\mathrm{SKE},A}$ additionally reflected the dynamic behavior of lateral vortices.
3. Classical descriptors such as DC_{60} and SC_{60} were less sensitive to higher frequency, small-scale vortex dynamics, confirming the added value of the advanced parameters introduced.
4. The CFD results and the experiment data agree well. Strong flow separation will reduce the model's accuracy.

The coupled intake and LPC simulation showed a clear upstream influence of the LPC on intake flow dynamics

1. A frequency shift of the large central flow separation's (SB) first modal frequency from 15.7 to 25.1 Hz and the emergence of a new low-frequency mode at 6.3 Hz related to the lateral vortices is caused by the LPC coupling.
2. A new dominant SB mode at 75.2 Hz, not observed in the isolated intake, indicating an induced amplification of lateral vortex systems through LPC interaction is found.
3. The most dominant frequency of the SB at 150.4 Hz was confirmed and matches experimental observations, highlighting the robustness of the numerical approach.
4. At certain periods (e.g., $t = 0.1649$ s), the vortex cores of SB split, which is indicated by a drop in $c_{\mathrm{SKE},A}$ and the distorted mass flow ratio ($\mu_{\Upsilon,di}$).

Across all parameters, the temporal variations remained small relative to the mean values, but the frequency content analysis highlighted that specific modes can strongly affect flow inhomogeneity and potential engine performance risks. A complete spectrum of the dominant frequencies of aerodynamic phenomena could not be found without coupling the LPC. The parameters for quantifying flow distortion are variable over a period of time. Potential maximum values would be ignored in a steady-state analysis and could affect engine performance.

Given the flow field at the intake outlet, the specific frequency, location and phenomenon can be precisely determined. By understanding which frequencies and locations in the intake flow negatively affect engine performance, the intake geometry can be systematically optimized to avoid or mitigate these effects. By adjusting the intake design, weaknesses in the system can be specifically addressed and the performance of the engine can be improved.

Acronyms

AIP	Aerodynamic Interface Plane
CFD	Computational Fluid Dynamic
DIP	Duct Inlet Plane
DOP	Duct Outlet Plane
FR	Frozen Rotor
IA	Induced Amplification
LPC	Low Pressure Compressor
LV	Lateral Vortices
MEIRD	Military Engine Intake Research Duct
MP	Mixing Plane
MS	Modal Shift
PR	Pressure Recovery
PSD	Power Spectral Density

RANS	Reynolds Averaged Navier Stokes
SAE	Society of Automotive Engineers
SB	Flow Separation Bubble
SKE	Secondary Kinetic Energy
UAS	Unmanned Aerial Systems

Nomenclature

Symbols

β, γ, δ	Local magnitude [-]
ω	Vorticity [1/s]
B	Perimeter [m]
b	Perimeter coordinate [m]
d	Diameter [m]
f	Frequency [1/s]
l	Length [m]
L	Cross-sectional load [N/m]
μ	Mass flow ratio [-]
p	Pressure [Pa]
n	Spool speed [-]
s	Centerline [-]
St	Strouhal number [-]
v	Velocity [m/s]
Ma	Mach number [-]
Re	Reynolds number [-]
DC_{60}	Distortion coefficient [-]
SC_{60}	Swirl coefficient [-]
SKE	Secondary kinetic energy [Pa]
TKE	Turbulence kinetic energy [J/kg]
rev	Revolutions [-]

Superscripts and subscripts

A	Area (integral)
cl	Clean
di	Distorted
i	Intake
In	Inlet conditions
Qx	Cross-section x
rel	Relative
sec	Secondary flow component
Sxx	Angular sector xx of the cross-sections
t	Stagnation
Υ	Ratio limiter
ξ, η, ζ	Local coordinates aligned with $\overline{v}_Q$
φ	Local polar coordinate on the cross-section

Funding sources

This research did not receive any specific grant from funding agencies in the public, commercial, or not-for-profit sectors. The work was carried out within the regular research activities of the Institute of Jet Propulsion, University of the Bundeswehr Munich.

Competing interests

Andreas Grois declares that he has no conflict of interest. Luis Oberthür declares that he has no conflict of interest. Julian Scheibel declares that he has no conflict of interest. Marcel Stößel declares that he has no conflict of interest. Dragan Kožulović declares that he has no conflict of interest. Michael Krummenauer declares that he has no conflict of interest.

References

Berens T. M., Delot A.-L., Chevalier M., and van Muijden J. (2014). Numerical simulations for high offset intake diffuser flows. In: 52nd AIAA Aerospace Sciences Meeting, AIAA 2014-0371. National Harbor, MD, USA: American Institute of Aeronautics and Astronautics.

Bowditch D. N., and Coltrin R. E. (1983). A survey of inlet/engine distortion compatibility. In: 19th Joint Propulsion Conference, AIAA 83-1166. Seattle, WA, USA: American Institute of Aeronautics and Astronautics.

Brehm S., Kächele T., and Niehuis R. (2014). CFD investigations on the influence of varying inflow conditions on the aerodynamics in an S-shaped inlet duct. In: 50th AIAA/ASME/SAE/ASEE Joint Propulsion Conference, AIAA 2014-3595. Cleveland, OH, USA: American Institute of Aeronautics and Astronautics.

Callahan G. M., and Stenning A. H. (1971). Attenuation of inlet flow distortion upstream of axial flow compressors. *Journal of Aircraft*. 8 (4): 227–233. https://doi.org/10.2514/3.44259.

Chahl J. (2015). Unmanned aerial systems (UAS) research opportunities. *Aerospace*. 2 (2): 189–202. https://doi.org/10.3390/aerospace2020189.

Fiola C., and Agarwal R. K. (2015). Simulation of secondary and separated flow in diffusing S ducts. *Journal of Propulsion and Power*. 31 (1): 180–191. https://doi.org/10.2514/1.B35275.

Garnier E. (2015). Flow control by pulsed jet in a curved S-duct: A spectral analysis. *AIAA Journal*. 53 (10): 2813–2827. https://doi.org/10.2514/1.J053422.

Granot E. (2019). Derivation of Euler's formula and $\zeta(2k)$ using the Nyquist–Shannon sampling theorem. *American Journal of Signal Processing*. 9 (1): 1–5.

Grois A., Stößel M., Kožulović D., and Krummenauer M. (2024). Effects of varying inflow conditions on the flow inhomogeneities along a highly bent intake duct. In: 26th International Symposium on Air Breathing Engines, Vol. 1, Toulouse, France. Indianapolis, Indiana, USA, 593–609.

Grois A., Stößel M., Krummenauer M., and Kožulović D. (2023). Novel inhomogeneity progression analysis of a highly bent intake. In: International Gas Turbine Congress 2023, IGTC 2023-31, Kyoto, Tokyo, Japan.

Grois A., Stößel M., Krummenauer M., Kožulović D., and Niehuis R. (2023). Impact of different flight conditions on the flow in a highly curved intake duct. In: Proceedings of the 15th European Conference on Turbomachinery Fluid Dynamics and Thermodynamics, ETC2023-129, Budapest, Hungary, Porto Recanati, Italy.

Hanrahan S. K., Scheibel J. A., Grois A., Stößel M., Kožul M., et al. (2025). An assessment of algebraic and differential reynolds-stress models for a highly-bent serpentine aircraft intake. In: ASME Turbo Expo 2025: Turbomachinery Technical Conference and Exposition, Vol. 11. Memphis, TN, USA: American Society of Mechanical Engineers. 1–16.

Haug J. P., and Niehuis R. (2017). Full annulus simulations of a transonic axial compressor stage with distorted inflow at transonic and subsonic blade tip speed. In: Proceedings of the 12th European Conference on Turbomachinery Fluid Dynamics and Thermodynamics, ETC2017-211, Stockholm, Sweden, Porto Recanati, Italien.

Haug J. P., Rademakers R. P. M., Stößel M., and Niehuis R. (2018). Numerical flow field analysis in a highly bent intake duct. In: ASME Turbo Expo 2018: Turbomachinery Technical Conference and Exposition, GT2018-76633. Oslo, Norway: American Society of Mechanical Engineers. 1–12.

Johansson M. (2006). Propulsion integration in an UAV. In: 24th AIAA Applied Aerodynamics Conference, AIAA 2006-2834. San Francisco, CA, USA: American Institute of Aeronautics and Astronautics.

Kim H. J., and Durbin P. A. (1988). Observations of the frequencies in a sphere wake and of drag increase by acoustic excitation. The Physics of Fluids. 31 (11): 3260–3265. https://doi.org/10.1063/1.866937.

Laird A. R., Rogers B. P., and Meyerand M. E. (2004). Comparison of fourier and wavelet resampling methods. *Magnetic Resonance in Medicine*. 51 (2): 418–422. https://doi.org/10.1002/mrm.v51:2.

Liu K., Wang H.-r., Chen Y.-c., Xie H., and Liu Z.-W. (2024). Comparison of DES and URANS: Estimation of fluctuating pressure from URANS simulations in stilling basins. *Journal of Hydrodynamics*. 36 (4): 609–623. https://doi.org/10.1007/s42241-024-0055-1.

Maghsoudi I., Vaziry M. A., and Mahmoodi M. (2020). Experimental investigation of flow and distortion mitigation by mechanical vortex generators in a coupled serpentine inlet-turbofan engine system. *Chinese Journal of Aeronautics*. 33 (5): 1375–1391. https://doi.org/10.1016/j.cja.2019.12.002.

Migliorini M., Zachos P. K., MacManus D. G., and Giannouloudis A. (2024). Effect of a fan on the unsteady distortion of S-duct intakes. In: 58th 3AF International Conference on Applied Aerodynamics, AERO2024-02-MIGLIORINI, Orléans, Paris, France.

Migliorini M., Zachos P. K., MacManus D. G., and Haladuda P. (2023). S-duct flow distortion with non-uniform inlet conditions. Proceedings of the Institution of Mechanical Engineers, Part G: Journal of Aerospace Engineering. 237 (2): 357–373. https://doi.org/10.1177/09544100221101669.

Nikitin N. V., Popelenskaya N. V., and Stroh A. (2021). Prandtl's secondary flows of the second kind. problems of description, prediction, and simulation. *Fluid Dynamics*. 56 (4): 513–538. https://doi.org/10.1134/S0015462821040091.

Piovesan T., Migliorini M., Zachos P. K., and Tsoutsanis P. (2024). Dynamic swirl distortion characteristics in S-shaped diffusers using UCNS3D and time-resolved, stereo PIV methods. In: AIAA SCITECH 2024 Forum, AIAA 2024-1196. Orlando, FL, USA: American Institute of Aeronautics and Astronautics.

Rademakers R. P. M., Bindl S., and Niehuis R. (2016). Effects of flow distortions as they occur in S-duct inlets on the performance and stability of a jet engine. *Journal of Engineering for Gas Turbines and Power*. 138 (2): 022605-1–022605-10. https://doi.org/10.1115/1.4031305.

Rademakers R. P. M., Probst H., Schneider T., and Niehuis R. (2018). Experimental investigations on a bent engine inlet duct coupled with a turbofan engine. In: 56th AIAA Aerospace Sciences Meeting, AIAA 2018-1353. Kissimmee, FL, USA: American Institute of Aeronautics and Astronautics.

Rademakers R. P. M., Stößel M., Kožulović D., and Niehuis R. (2024). On intake-compressor interactions within an integrated propulsion system. In: ASME Turbo Expo 2024: Turbomachinery Technical Conference and Exposition, GT2024-128168. London, UK: American Society of Mechanical Engineers. 1–15.

Remiger J., Grois A., Stößel M., Kožulović D., and Krummenauer M. (2024). Impact of various intake configurations on the flight mission performance of an unmanned aircraft. In: ASME Turbo Expo 2024: Turbomachinery Technical Conference and Exposition, Vol. 1. London, UK: American Society of Mechanical Engineers. 1–11.

Rütten F., Schröder W., and Meinke M. (2005). Large-eddy simulation of low frequency oscillations of the dean vortices in turbulent pipe bend flows. *Physics of Fluids*. 17 (3): 035107-1–035107-11.

SAE International (2011). Gas turbine engine inlet flow distortion guidelines, Aerospace Recommended Practice ARP1420B, SAE International. Reaffirmed July 2011; revised February 2002.

SAE International (2017). Inlet total-pressure-distortion considerations for gas-turbine engines, Aerospace Information Report AIR1419C, SAE International.

SAE International (2022). A methodology for assessing inlet swirl distortion, Aerospace Information Report AIR5686, SAE International. Reaffirmed March 2022.

Sakamoto H., and Haniu H. (1990). A study on vortex shedding from spheres in a uniform flow. *Journal of Fluids Engineering*. 112 (4): 386–392. https://doi.org/10.1115/1.2909415.

Scheibel J., Schäfer Y., Stößel M., and Kožulović D. (2022). Numerical simulation of the complete component of the real engine with/without control, Project Report T2.3, ACONIT – Actuators for Surge Control in Gas Turbines.

Scheibel J. A., Stößel M., and Kožulović D. (2024). Influence of engine conditions on the performance prediction of a two-stage transonic low pressure compressor. In: ASME Turbo Expo 2024: Turbomachinery Technical Conference and Exposition, GT2024-126672. London, UK: American Society of Mechanical Engineers. 1–12.

Silva-Leon J., and Cioncolini A. (2019). Effect of inclination on vortex shedding frequency behind a bent cylinder: An experimental study. *Fluids*. 4 (2): 100. https://doi.org/10.3390/fluids4020100.

Smirnov P. E., and Menter F. R. (2009). Sensitization of the SST turbulence model to rotation and curvature by applying the spalart–shur correction term. *Journal of Turbomachinery*. 131 (4): 041010-1–041010-8. https://doi.org/10.1115/1.3070573.

Soeder R. H., and Bobula G. A. (1979). Effect of steady-state pressure distortion on flow characteristics entering a turbofan engine. Technical Memorandum NASA TM-79134. Cleveland, OH, USA: National Aeronautics and Space Administration. https://ntrs.nasa.gov/citations/19790015798.

Stevens C. H., Spong E. D., and Hammock M. S. (1978). F-15 inlet/engine test techniques and distortion methodologies studies. Volume I: Technical discussion. Contractor Report NASA CR-144866. National Aeronautics and Space Administration. https://ntrs.nasa.gov/citations/19780022180.

Stößel M. (2017). Umsetzung und Erprobung eines Ejektor-Einblasesystems zur Stabilisierung des Niederdruckverdichters am Turbostrahltriebwerk Larzac 04. PhD thesis, Universität der Bundeswehr München.

Tanguy G., MacManus D. G., Garnier E., and Martin P. G. (2018). Characteristics of unsteady total pressure distortion for a complex aero-engine intake duct. *Aerospace Science and Technology*. 78: 297–311. https://doi.org/10.1016/j.ast.2018.04.031.

Xiong L., Sugimoto R., and Quaranta E. (2019). Effects of turbofan engine intake droop and length on fan tone noise. In: 25th AIAA/CEAS Aeroacoustics Conference, AIAA 2019-2581. Delft, The Netherlands: American Institute of Aeronautics and Astronautics.